Electrochimica Acta 233 (2017) 1–12

Contents lists available at ScienceDirect

Electrochimica Acta

journal homepage: www.elsevier.com/locate/electacta

The impact of high-frequency-high-current perturbations on film formation at the negative electrode-electrolyte interface

Kotub Uddin[a,*], Limhi Somerville[b], Anup Barai[a], Michael Lain[a], T.R. Ashwin[a], Paul Jennings[a], James Marco[a]

[a] WMG, International Digital Laboratory, The University of Warwick, Coventry CV4 7AL, UK
[b] Jaguar Land Rover, Banbury Road, Warwick CV35 0XJ, UK

ARTICLE INFO

Article history:
Received 17 November 2016
Received in revised form 2 March 2017
Accepted 3 March 2017
Available online 7 March 2017

Keywords:
High frequency current
Lithium ion
Degradation
Cell autopsy
Electrochemical modelling

ABSTRACT

Long term ageing experimental results show that degradation resulting from coupled DC and AC current waveforms lead to additional degradation of lithium-ion batteries above that experienced through pure DC cycling. More profoundly, such experiments show a dependency of battery degradation on the frequency of AC perturbation. This paper addresses the underlying causality of this frequency dependent degradation. Cell autopsy techniques, namely X-ray photoelectron spectroscopy (XPS) of the negative electrode surface film, show growth of surface film components with the superimposition of an AC waveform. XPS results show that high frequency AC perturbations lead to the increased formation of a passivating film. In order to determine the cause of this increased film formation, a heterogeneous electrochemical model for the $LiNiCoAlO_2/C_6$ lithium ion battery coupled with governing equations for the electrical double-layer and solid electrolyte interface film growth is developed. Simulation results suggest that the increased growth of surface film is attributed to frequency dependent heat generation. This is due to ion kinetics in the double layer which are governed by the Poisson-Boltzmann equation. Additional thermal and reference cell relaxation experiments are undertaken that further corroborates the conclusion that heat generation within the battery is a function of the AC excitation frequency through resistive dissipation and the entropy of the cell reaction.

1. Introduction

Lithium-ion (li-ion) cells are recognised as a central technology in the process of achieving a clean and sustainable energy future through the electrification of road transport and the use of grid-connected energy storage to underpin the increased use of renewable energy sources [1,2]. Within each application, a key enabling technology is the design and integration of the power electronic subsystems that are required to manage the flow of energy [3]; such subsystems are known to generate undesired electrical noise [4–6]. For example, Fig. 1 shows the current waveform from charging a Nissan Leaf vehicle using a commercially available 3 kW Eltek Valere bi-directional vehicle charger. Fig. 1 highlights the measured harmonic content present on the electrical input to the battery.

High frequency current oscillations, or ripple, if unhindered will add a further perturbative load onto the vehicle's battery system. In recent work, Uddin et. al. [7] measured the electrical noise on the DC link of a high voltage bus on a pre-production series hybrid electric vehicle during a regenerative breaking event [7]. This data was used to define the current waveforms that batteries are exposed to during typical electric operation. Long term battery degradation resulting from cycling batteries under such waveforms was studied in [7]. The authors show that exposing the battery to coupled direct current (DC) and alternating currents (AC) lead to additional battery degradation that is related to the frequency of the perturbative ripple current. Through the experimental data presented, the authors were able to quantify the impact of AC excitation at the cell-level. However, the authors were not able to provide any reasoning for the battery degradation. Furthermore, given the novelty of the result presented [7], it was not possible to explain the causality of degradation due to AC ripple excitation directly from literature.

This paper extends the research presented in [7] by seeking to explain the underlying causality of degradation resulting from high frequency ripple current. This is achieved through a combination of further experimental analysis and novel mathematical modelling.

* Corresponding author. Tel.: +44 0 2476 150 736; fax: +44 0 2476 524 307.
E-mail address: k.uddin@warwick.ac.uk (K. Uddin).

http://dx.doi.org/10.1016/j.electacta.2017.03.020

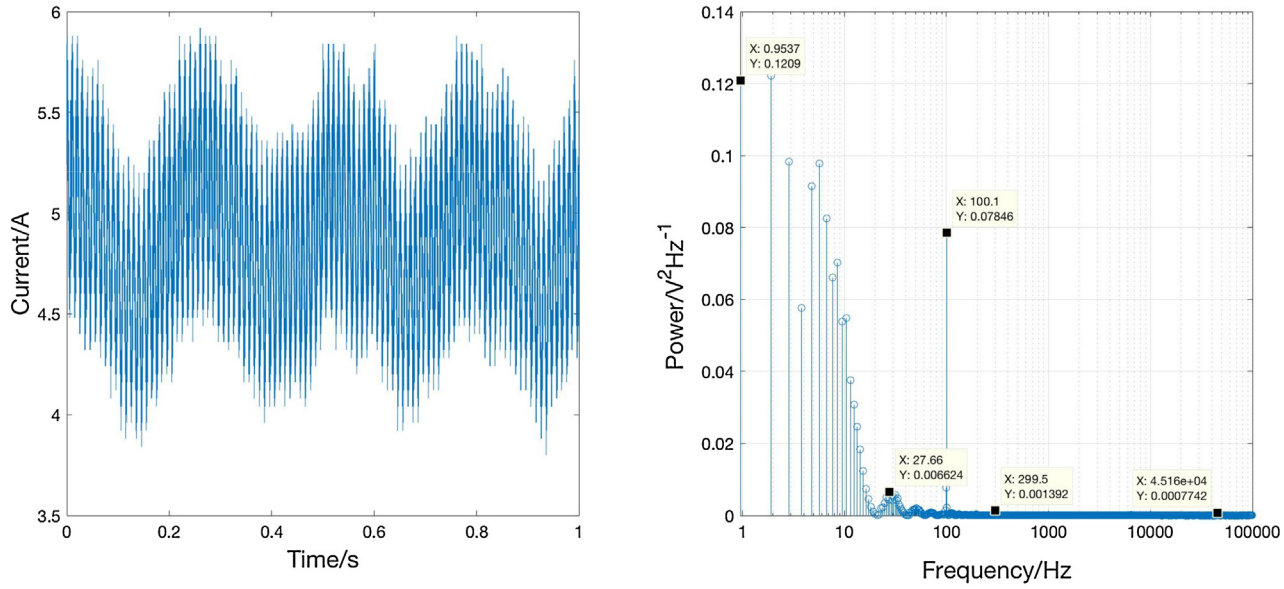

Fig. 1. The left hand panel shows the measurement of a coupled DC-AC current. The scope settings were: 100ms per division, with 10^6 samples taken per second. The right hand panel is the power spectrum of the measured current.

X-ray photoelectron spectroscopy (XPS) is employed to study the degraded cells used in our previous work [7]. A heterogeneous electrochemical model based on continuum theory has been developed and used to investigate the dependency of cell degradation on the frequency of an AC perturbation. The model relates battery degradation to the frequency dependant heat generation in the electrical double layer resulting from super-imposed AC loads which is known to promote more pronounced growth of solid electrolyte interface (SEI) film [8]. Thermal and reference electrode relaxation experiments are presented that demonstrate the processes involved, to further understand and explain battery degradation when the cell is exposed to AC current excitation.

This paper is structured as follows: in the next section, experimental methodologies pertaining to results presented in this paper are agglomerated and presented. In Section 3, a heterogeneous electrochemical model that accounts for ion dynamics in the electrical double-layer through the Poisson-Boltzmann equation is presented. The model suggests that the cause of cell degradation under coupled AC and DC waveforms is the increased heat generation. The model results are substantiated by experimental results presented in Sections 4. Long term cell ageing test results, where cells were cycled 1200 times under an AC and DC coupled waveform, are presented; XPS autopsy results for these cells show a frequency dependant growth of surface film. Finally, in Section 5 we conclude and state further work.

2. Experimental

2.1. Long Term Ageing Test

It is beyond the scope of this paper to explain, in detail, the original experimental ageing study. This work is presented in [7]. A full description of the aims and objectives, the methods and equipment employed are presented. However, for completeness a brief summary is provided in this subsection, highlighting key aspects of the work.

Fifteen commercially available 3.0 *Ah* 18650-type cells were cycled [7]. Each cell had a LiC_6 negative electrode, $Li(Ni_{0.822}Co_{0.148}Al_{0.030})O_2$ (NCA) positive electrode, separated by a polyethylene separator, sandwiched between two current collectors and immersed in an electrolyte solution comprising of ethylene carbonate (EC), ethyl methyl carbonate (EMC), vinylene carbonate (VC) and $LiPF_6$ salt.

Each cell was cycled using a DC current signal (I_{DC}) super-positioned with an AC perturbation $I_{AC}\sin(\omega t)$ such that the overall current (I) waveform was:

$$I = I_{DC} + I_{AC}\sin(\omega t) \tag{1}$$

with a resulting cell potential:

$$V = V_{DC} + V_{AC}\sin(\omega t - \theta) \tag{2}$$

where θ is a phase shift between the cell potential and current waveform. The test signals were generated using a bespoke amplifier to generate the AC waveform and a Bitrode cell cycler to generate the DC load profile. In addition, a Tektronix non-contact current probe and oscilloscope was used for data acquisition and test monitoring. A LAUDA heating and cooling system was used to ensure that the ambient temperature was maintained at 25°C.

The DC portion of the cycle started with a $0.8C_{cycle}$ discharge (where C_{cycle} is the de-rated battery C-rate, i.e., the value of retained discharge capacity after an ageing characterisation test) from 95% SOC_{cycle} to 65% SOC_{cycle} (where SOC_{cycle} is the state of charge defined by C_{cycle}). Following a rest period of 10 minutes, each cell was then charged using a standard Constant Current–Constant Voltage (CC-CV) protocol, in which the cell was charged (CC) to the upper cell potential limit of 4.1 *V*(corresponding to 95% SOC_{cycle}) at which point charging continued using a CV method until the value of current reduced to 0.15 A. Superimposed onto the DC cycle was one of four AC current excitations, of frequency: 10 *Hz*, 55 *Hz*, 254 *Hz* and 14.8 *kHz*–with a peak-to-peak current of $1.2C_{cycle}$. To improve the robustness of the test method and the efficacy of the results, three cells of the same type were exercised using each current waveform defined above.

Ageing characterisation was carried out after 300, 600, 900 and 1200 complete charge–discharge cycles. The characterisation tests involved a 1 C capacity retention tests; pulse power tests using 10 second pulses at 20%, 40%, 60%, 80% and 100% of the manufacturers recommended maximum continuous charge and discharge current at 90%, 50% and 20% state of charge (SoC); electrochemical impedance spectroscopy tests were also carried out at 90%, 50% and 20% SoC using a Solartron ModuLab EIS System.

2.2. Cell Autopsy

Three samples were taken from each cell, approximately 160 mm from the top of the latitudinal axis (where top is defined as the start of the jelly roll) along the first half of the length of the jelly roll as opened. This position was chosen in order to avoid the central band on the longitudinal axis of an 18650- type cell which has unusually high resistances attributed to poor electrode wetting [9]. This sample location also avoids the inner windings of the cell which is prone to de-lamination [9]. All three samples showed good agreement in peak positions and widths. To ensure that sample inhomogeneity does not affect results, a large elliptical was used equating to an analysed electrode area containing between 500 and 1000 graphite particles.

XPS provides information on the chemical environment of elemental species from the top <10 *nm* of a sample surface. Since electrode samples are usually covered with a number of deposits, in this work the sample was sputtered at 500 *eV* with an Ar^+ ion sputter gun for 90 seconds to remove the salts, solvents and deposits from the top of the electrode surface. The surface film was deemed ready for analysis if the relative peak areas after an episode of sputtering did not change. This same technique was employed in a recent study published in [9]. As shown in the work of Somerville et. al., it is possible to determine the total contribution to the chemical environments of the surface film (e.g., C-O, because it surrounds the active material particles compared to graphite C-C), providing a relative surface film thickness [9]. After acquisition, all spectra were referenced to the C 1*s* peak at 284.4 *eV* (after sputtering). The peaks were assigned using Shirley backgrounds and mixed Gaussian-Lorentzian (Voigt) line shapes.

Samples were analysed in duplicate with a Kratos Axis Ultra DLD spectrometer and a Thermo k-alpha$^+$ spectrometer. Both maintained a base pressure of circa. 2×10^{-10} mbar during analysis. XPS measurements were performed using a monochromatic Al k_α x-ray source and conducted at room temperature at a take-off angle of 90° with respect to the parallel surface. The core level spectra were recorded using a pass energy of 20 eV (resolution approx. 0.4 *eV*), across an elliptical area of circa. 300 $\mu m \times 700\ \mu m$.

2.3. Cell Potential Relaxation

Cell potential relaxation in the electrolyte adjacent to the electrode was investigated using three electrode cells containing three lithium metal electrodes (working, counter and reference). Lithium electrodes were preferred over intercalation electrode materials because if the latter had been used, the cell potential relaxation transient would also reflect solid state diffusion, either towards or away from the particle surface. The Swagelok® three electrode cells, which were used for this test, contained three layers of separator; a glass fibre layer (GF/A) to minimise the risk of dendrites, with porous polyethylene layers on either side. The electrolyte was 1 *mol* dm^{-3} $LiPF_6$ in EC:EMC (3:7), with a 2 *wt%* (weight percentage) VC.

The cells were tested on a Bio-Logic VMP3 multi-channel potentiostat. After some conditioning charge and discharge pulses, individual tests were used for each measurement. A single frequency galvanostatic impedance was performed, with an applied current of +0.1 *mA* cm^{-2} or −0.1 *mA* cm^{-2}. The four single frequencies used were selected to match the other experiments i.e. 10 *Hz*, 55 *Hz*, 254 *Hz* and 14.8 *kHz*. The number of repeat measurements was adjusted in the range 300–500. The AC perturbation was applied for one minute in each case. The cell potential relaxation curves following the AC perturbation were then compared for the four frequencies.

Cell potential relaxation experiments are used to further deduce information on ion concentration at the electrode-electrolyte boundary which is known to impact heat generation though the heat of mixing. Experimental results from this stage of the research are presented in and discussed in Section 6.3.

3. Theory

In this section, we develop an electrochemical model that accurately describes the high frequency dynamics on a lithium ion battery. This model is then employed to understand the theoretical impact of coupled AC and DC waveforms on lithium ion battery degradation within the context of electrochemistry theory.

3.1. Model formulation

Within the field of electrochemical energy storage, Doyle Fuller and Newman's model [19] based on principles of transport phenomena, electrochemistry and thermodynamics is well established. The model solves for the electrolyte phase concentration:

$$\frac{\partial(\varepsilon_e c_e)}{\partial t} = \nabla \cdot \left(D_e^{eff} \nabla c_e\right) + \frac{1 - t_+^0}{F} a_s j \tag{3}$$

solid phase concentration:

$$\frac{\partial(\varepsilon_s c_s)}{\partial t} = \frac{D_s}{r^2}\frac{\partial}{\partial r}\left(r^2 \frac{\partial c_s}{\partial r}\right) \tag{4}$$

electrolyte phase potential:

$$\nabla \cdot \left(\kappa_e^{eff} \nabla \phi_e\right) + \nabla \cdot \left[\kappa_{e,D}^{eff} \nabla \ln(c_e)\right] = -a_s j \tag{5}$$

and solid phase potential:

$$\nabla \cdot \left(\sigma_s^{eff} \nabla \phi_s\right) = a_s j \tag{6}$$

where c is concertation, ϕ is the electrode potential, ε is porosity, D^{eff}, σ^{eff} and k^{eff} are the effective diffusion coefficient, conductivity and charge transfer coefficient, respectively, t_+^0 is the transference number, a_s is the specific surface area of the electrode and j is the current density; the subscripts e and s denote the electrolyte and solid phase respectively. Doyle, Fuller and Newman's model consists of three primary domains (see Fig. 2): the negative electrode (in this work LiC_6), the separator (in this work polyethylene) and the positive electrode (in this work $LiNiCoAlO_2$) permeated by electrolyte solution. During electrical discharge, lithium ions that occupy interstitial sites with the LiC_6 electrode diffuse to the surface where they react (de-intercalate) and transfer from a solid into a liquid phase. The ions then diffuse and migrate through the electrolyte solution via the separator to the positive electrode where they react (intercalate) and occupy interstitial sites within the metal oxide material. During electrical charging the reverse reactions take place, in summary: lithium ions de-intercalate from the positive electrode (metal oxide) and intercalate within the negative electrode (carbon). Due to the widespread acceptance of the Doyle Fuller and Newman model, it suffices here to refer interested readers to Refs. [19–22] for more details of model formulation and boundary conditions.

In the Doyle Fuller and Newman electrochemical model the reaction kinetics are modelled by the Butler-Volmer equation

$$j = a_s j_0 \left\{ \exp\left[\frac{\alpha_a F}{RT}\eta\right] - \exp\left[\frac{-\alpha_c F}{RT}\eta\right] \right\} \tag{7}$$

where j_0 is the exchange current density, α_a and α_c are the charge transfer coefficients for the anode and cathode respectively, and η is the overpotential defined for the negative electrode (η_n),

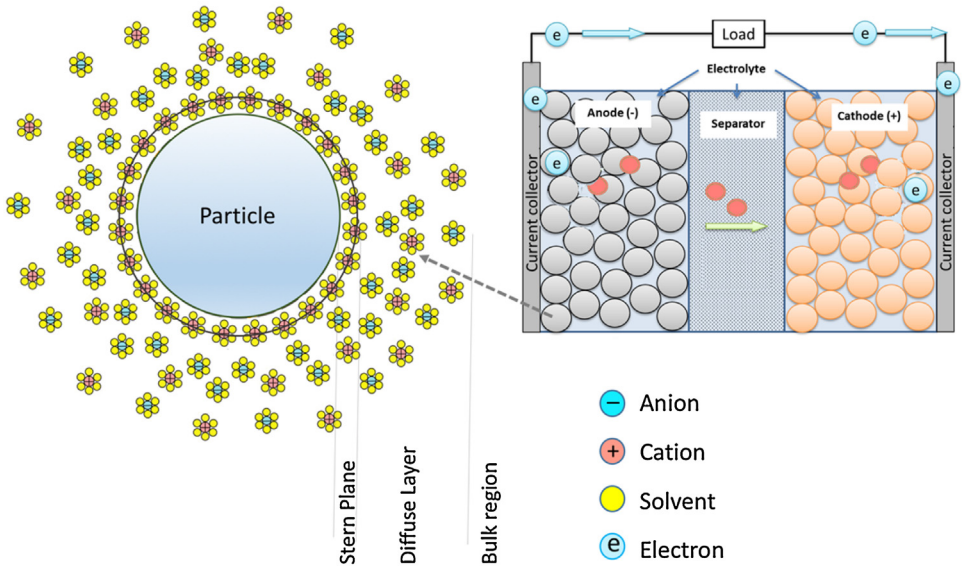

Fig. 2. Schematic of the domains considered in the Doyle Fuller and Newman electrochemical model (right hand side); the demarcation of this work is the consideration of the electrode double-layer around the electrode particle which consists of the diffuse layer and Stern plane (left hand schematic).

positive electrode (η_p) and SEI as (η_{SEI}) [23]:

$$\eta_n = \phi_s - \phi_e - U - \frac{R_{film}|_{Li^+}}{a_s} j \tag{8}$$

$$\eta_p = \phi_s - \phi_e - U \tag{9}$$

$$\eta_{SEI} = \phi_s - \phi_e - U_{ref} - \frac{R_{film}|_{e^-}}{a_s} j. \tag{10}$$

The passivating film resistance R_{film} is separated into electronic and ionic conurbations because the SEI layer is permeable to Li-ions but impermeable to electrolyte and electrons. On the other hand, the anodic reaction $x\mathrm{Li}^+ + xe^- + Li_{1-x}\mathrm{C}_6 \leftrightarrow \mathrm{LiC}_6$ takes place inside the electrode particle; the ions that participate in the reaction pass through the SEI reducing their electrical potential. This is represented by the last term in equation (8).

It is well understood that the Butler-Volmer equation (7) is unable, in the high frequency regime, to reproduce the coupled resistance and surface-capacitance behaviour observed in electrochemical impedance spectroscopy tests [20]. To address this issue, the authors extend the original model, employing the technique presented by Xiao and Choe [24]. The electrolyte adjoining the particle is divided into two regions: the bulk region and the double layer (DL) which itself is composed of the diffuse layer with a thickness of $1-10\,nm$ and the Stern plane with a thickness equal to the sum of the diameters of an anion and a solvent molecule [25]. A schematic diagram of these regions are depicted in Fig. 2. Lithium ions travel through the DL and participate in chemical reactions at the surface of the solid particles while the anions that do not take part in the chemical reactions are blocked outside of the Stern plane [24]. Due to the ensuing electrolyte potential, the DL region is assumed not to be charge neutral while the bulk is charge neutral. Furthermore, the transport of cations (lithium ions) and anions (PF6-) in the DL is assumed to be governed by their respective local chemical potential gradients determined by electrostatic potentials and ion concentration gradients. In this formulation, ion kinetics in the DL region is governed by the Poisson-Boltzmann equation

$$\nabla^2 \phi_{DL} + \frac{F}{E}(c^+ - c^-) = 0 \tag{11}$$

where E is the permittivity of dielectric solvent, F is Faraday's constant and the subscripts + and – relate to cation and anion respectively. Charge conservation is given by

$$\frac{\partial(c_{DL}^{\pm})}{\partial t} = \frac{\beta^{\pm}}{Fr^2}\frac{\partial}{\partial r}\left(r^2 c_{DL}^{\pm}\frac{\partial \mu_{DL}^{\pm}}{\partial r}\right) \tag{12}$$

where the subscript DL denotes the double layer, β is the ion mobility and μ is the chemical potential defined as

$$\mu_{DL}^{\pm} = \pm F\phi_{DL} + RT\ln(c_{DL}^{\pm}). \tag{13}$$

Instead of electroneutrallity, as assumed by Doyle, Fuller and Newman for the bulk region, here the Poisson-Boltzmann equation is used to calculate the chemical potential given in equation (13). For more detailed discussion on the derivation of equations (11)-(13), readers are directed to Ref. [24]. Model parameters used in this study are provided in the Appendix.

3.2. Numerical Method

To solve the system of equations (3) - (13), a finite volume based discretisation is adopted due to the inherent advantage that the boundary conditions can be applied non-invasively. The electrochemical variables are defined at the control volume centre and solved sequentially to evaluate the battery characteristics for multiple charge-discharge cycles. Each AC period is divided into 40 time steps, such that the time intervals for frequencies 10 Hz, 55 Hz, 254 Hz, and 1480 Hz are 2.5ms, 0.455ms, 0.098ms, and 0.0169ms, respectively. Load current is assumed constant within each time interval while the values of different time steps follow the AC + DC profile. The resulting matrix of equations are solved sequentially at each Cartesian nodal point while the solid phase lithium concentration (equation (4)) and DL species conservation (equation (12)) are solved at radial coordinates to give a pseudo two dimensional dependency. The equations are coupled together with Poisson-Boltzmann kinetics (equation (11)). The equations

are iterated until the residual error reduces to below the specified threshold value. This study assumes 1.0×10^{-03} A/cm^3 as the error limit for current densities on both electrodes.

3.3. Electrochemical model results

During operation, a battery typically works at cell potentials beyond the thermodynamic stability range of the organic electrolyte. Therefore, electrolyte decomposition, which includes the oxidation and reduction of electrolyte on the surface of the cathode and anode occurs. The factors affecting the subsequent SEI layer formation on the negative electrode include carbon substrate, electrolyte composition, additives and temperature [26]. Assuming that the pertinent cause of degradation is the increase in passivating surface film–as will be demonstrated in Section 4–and given that the cells used in the study were identical, i.e., carbon substrate, electrolyte composition and additives were the same; it is postulated that discrepancies in battery degradation resulted from varying heat generation rates that were present when the cells were excited by different waveforms.

The cell potential response and cation concentration in the stern plane under a current load of the form of equation (1) with varying frequencies is shown in Fig. 3. Ion kinetics is driven by the chemical potential μ (c.f., equation (13)) which includes both concentration and potential terms. Under the AC-DC coupled waveforms considered in this work, the gradient of the chemical potential is always one-directional, i.e., either positive or negative. Since the potential gradient is increasing, the amplitude of the oscillating concentration in the stern plane is also increasing (though not visible in Fig. 3 due to the short time increment presented). With regards to cell potential, the discrepancy in the amplitude of the cell potential response when galvanostatic waveforms with different frequencies are applied on a cell results from frequency dependant impedance of the electrochemical system.

The Butler-Volmer equation governs ion kinetics in the low frequency regime (< 1 *Hz*); the Poisson-Boltzmann equation on the other hand governs high frequency kinetics in the DL region and hence also the dependency of heat generation on frequency when $\omega \geq 10$ *Hz*. The simulated heat generation in the DL is shown in Fig. 4, which highlights differences in simulated heat generation arising from current perturbations of different frequencies. The heat generation is caused by the deviation of the surface overpotential from the equilibrium state, i.e., resistive dissipation.

Local heat generation p[W/cm] of both ions in DL is calculated as the product of chemical potential gradient and ion flux:

$$p_{DL}^{\pm} = 4\pi r^2 \frac{\partial \mu_{DL}^{\pm}}{\partial r} \cdot N_{DL}^{\pm} \tag{14}$$

where the ion flux in the double layer $N_{DL}^{\pm}$ [mol/s/cm^2] is given by [24]:

$$N_{DL}^{\pm} = -\frac{\beta_{\pm}}{F} \cdot c_{DL}^{\pm} \cdot \frac{\partial \mu_{DL}^{\pm}}{\partial r} \tag{15}$$

where β ion mobility. The heat generation for the whole cell can then be obtained by integration of $p_{DL}^{\pm}$. The cation flux N_{DL}^{+}, which is similar for all four frequencies, is determined by load current. The lithium ion chemical potential μ_{DL}^{+} however, can be different between frequencies because it is affected by the electrostatic potential ϕ_{DL} which interacts with anion concentration. The extra heat generation of lithium ion at 14.8 kHz is thus caused by the higher electrostatic potential ϕ_{DL} induced by the transient processes of anions in the DL.

The modelling results show that, for the NCA/C$_6$ cell studied in this work, a perturbation frequency of 14.8 *kHz* leads to the largest heat generation. Furthermore, while a perturbative frequency of 254 *Hz* generates larger anion sourced heat than $\omega < 254$*Hz*, the total heat generation is dominated by the dynamics of the cations; heat generation due to anions is consequently marginalised.

For the cell considered in this study, the ion mobility β_+ is $3.24 \times 10^{-10}\, cm^2V^{-1}s^{-1}$ and β_- is $1.85 \times 10^{-10}\, cm^2V^{-1}s^{-1}$. The magnitude of cation flux is thus larger than the anion flux. This is related to the larger reservoir of cations in the electrode, facilitating a relatively more sustainable cation flux compared with anion flux. The concentration of anions in the double layer on the other hand is larger than cation concertation, as found in Ref. [24].

Electrochemical modelling results presented in this section suggest that heat generated due to resistive dissipation within the DL is related to ion kinetics (i.e., AC excitation frequency) described by the Poisson-Boltzmann equation. Since heat is known to accelerate the growth of SEI, the modelling results are used to postulate that the growth of SEI film is dependent on the frequency of an AC perturbation. In the next section, experimental results are presented to verify the frequency dependant growth of SEI.

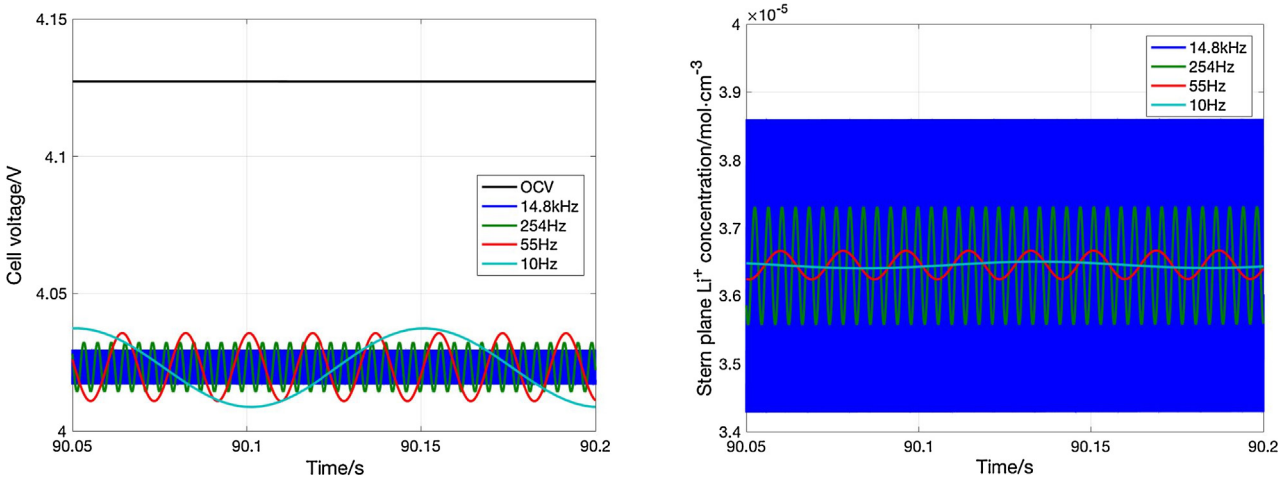

Fig. 3. The left hand panel shows cell potential response to a current perturbation of the form $I_{DC} + I_{AC}\sin(\omega t)$. The right hand panel shows lithium concentration in the stern plane as a function of time.

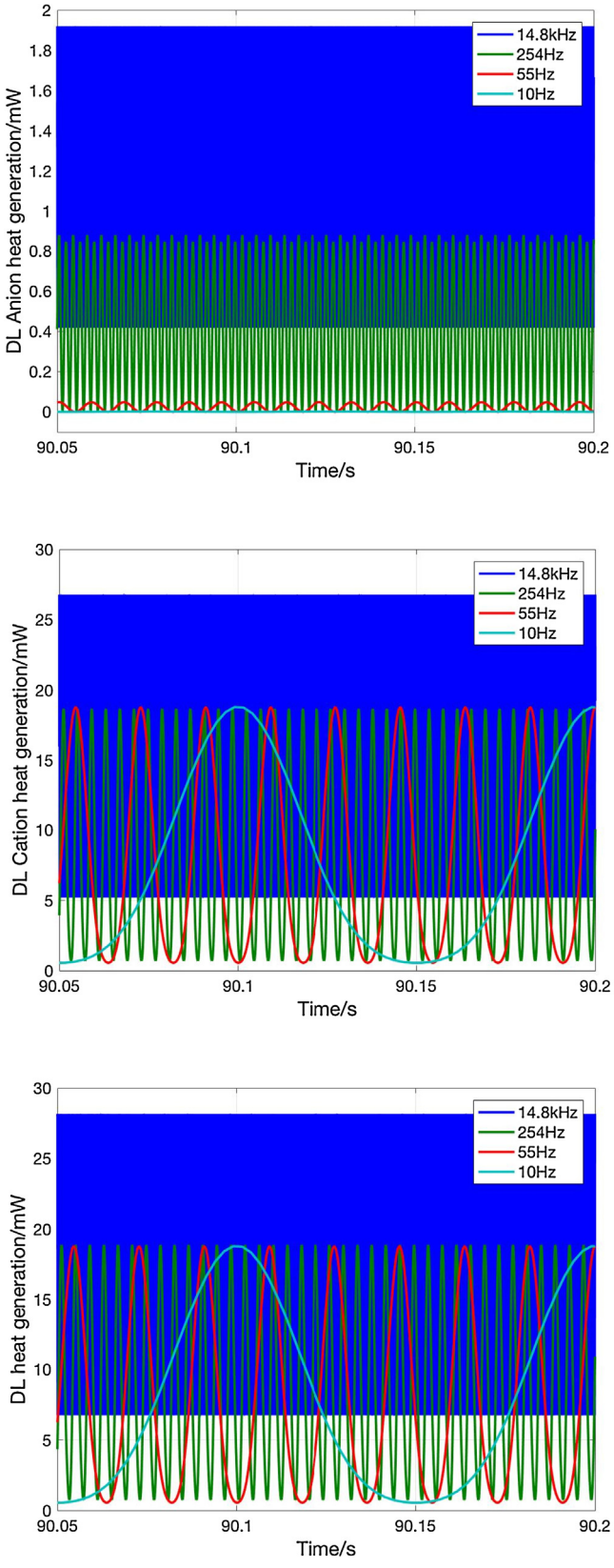

Fig. 4. Showing heat generation from anion kinetics (top panel), cation kinetics (middle panel) and total heat generation in the double layer.

4. Results and Discussion

4.1. Long Term Ageing Test Results

Electrochemical impedance spectroscopy (EIS) results comparing test cells prior to cycling and after 1200 cycles are shown in Fig. 5. The results presented in Fig. 5 are for single cells with the median value for resistance rise from the subset of cells in each frequency band [7]. Using analogies with electrical circuit models, the pronounced additional semi-circle in the high frequency region of the Nyquist plot for the 254 *Hz* and 14.8 *kHz* AC excitations indicate that there is an additional increase in resistance coupled with surface layer capacitances compared with the case of 55 *Hz*, 10 *Hz*and pure *DC* cycling.

The fall in 1 C discharge capacity and the rise in resistance are shown in Fig. 6. Capacity and power fade due to superpositioned AC perturbations with a frequency of 55 *Hz* and 10 *Hz* are only marginally different from pure DC cycling. On the other hand, at higher frequencies (14.8 *kHz*), there is an additional circa. 2.5% and 5% capacity and power fade respectively. Given that automotive end of life is defined by 20% capacity fade and a doubling of impedance [10–12], higher frequency AC perturbations can result in an extra 12.5% loss of useful capacity and 5% loss of required power compared with lower frequency AC perturbations, potentially shortening the operational lifetime of an automotive battery by up to one-and-a-half years [13].

The broad observation that coupling an AC perturbation to a DC load causes more battery degradation than a pure DC load is clear, since the energy throughput (E_{thro}) under a galvanostatic load of the form (1) is:

$$\begin{aligned} E_{thro} &= I_{DC}V_{DC}t - I_{AC}V_{DC}\frac{\cos(\omega t)+}{\omega} \\ &+I_{DC}V_{AC}\frac{\sin(\theta)\sin(\omega t) - \cos(\theta)\cos(\omega t)}{\omega} \\ +I_{AC}V_{AC}&\left(\frac{\cos(\theta)t}{2} - \frac{\cos(\theta)\sin(2\omega t) + \sin(\theta)\cos(2\omega t)}{4\omega}\right), \end{aligned} \tag{16}$$

In a high frequency regime ($\omega >> 1$), equation (3) reduces to

$$E_{thro} \cong I_{DC}V_{DC}t + I_{AC}V_{AC}\cos(\theta)\frac{t}{2} \tag{17}$$

which is dependent on frequency through the phase angle θ (as will be shown in Section 6). Equations (16) and (17) clearly demonstrate that electrical energy throughput is higher when AC waves are superimposed onto DC loads (i.e., when $I_{AC} \neq 0$ and $-\pi/2 < \theta < \pi/2$). The correlation between increased energy throughput and increased battery degradation is well established [14]. In this sense, the result that coupling an AC excitation to a DC load leads to increased degradation conforms with well-established theory. It is important to note however, that energy throughput is not the only stress factor which accelerates battery degradation. Elevated cell temperature is known to result in more severe degradation modes [8]. Arguably, the more noteworthy result–in terms of novelty–is the dependency of battery degradation on frequency when $I_{Ac} \neq 0$. The remainder of this paper explores this dependency further.

While the results presented in Figs. 5 and Fig. 66, at a component level, show that coupled AC perturbations lead to a level of degradation that exceeds that experienced with DC cycling in isolation, the frequency dependency of this degradation and fundamental causes of degradation are not yet fully understood. In the following subsection, post mortem examination of the cycled cells is presented to elucidate the mechanism of degradation exacerbated by superpositioning AC cycling.

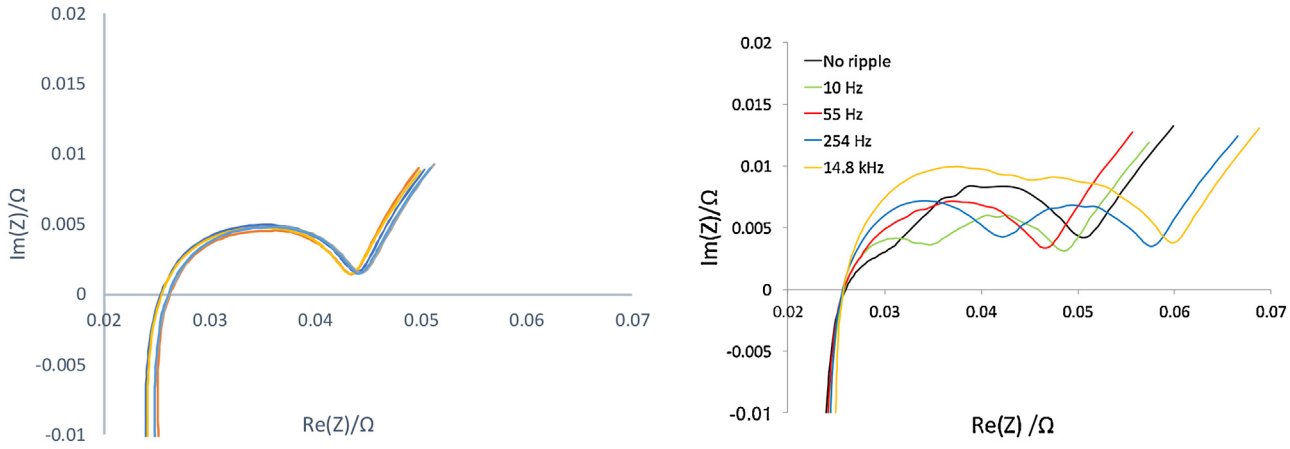

Fig. 5. The left hand panel shows initial EIS results for all cells measured at 50% SOC; the right hand panel shows EIS results for cells at different frequencies after 1200 cycles.

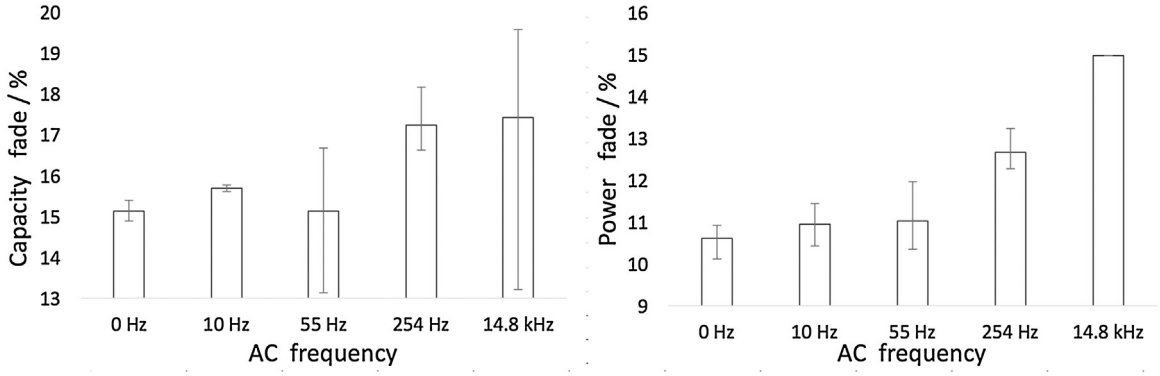

Fig. 6. The left hand panel shows average 1 C capacity fade after 1200 cycles; the right hand panel shows average power fade (impedance rise) results for cells at different frequencies after 1200 cycles. The error bars indicate the maximum and minimum measured values. For added confidence, these measurements were carried out twice, once using the Bitrode cell cycler and a second time using the Maccor 4200 Model cell cycler; the results for each cell was the same to within the error of the equipment. For 14.8 *kHz*, only a single cell was able to respond to the pulse current, so no error bars are shown.

4.2. XPS Cell Autopsy Results

To characterize the surface film formation resulting from DC-AC coupled cycling, XPS analysis was completed on the graphite electrodes of four cells–(a) a control sample cell that was not cycled, (b) a cell after 1200 DC and AC coupled cycles at 10 Hz, (c) a cell after 1200 DC and AC coupled cycles at 55 Hz and (d) a cell after 1200 DC and AC coupled cycles at 14.8 kHz. The XPS results for the C 1s spectra are presented in Fig. 7. The assignment of chemical environments are consistent with those found in literature [15–17]. Fig. 8 shows the area for the non-graphite chemical environments (concentration) relative to the frequency of the AC ripple. However, it excludes the Li-C component in the cells. This is because Fig. 7 shows a large Li-C component in the 'new cell' compared to all subsequent cells. It has been proposed that Li-C is formed from reaction of dimethyl carbonate with Li^+ followed by a radical induced chain reaction with lithium that is facilitated by the presence of H_2O and thus would primarily form directly after manufacture [17]. This work supports that assertion by showing a much higher quantity of Li-C in the new cell and lower concentrations in each subsequent cell after testing. However, when the Li-C peak is included in calculating the percentage of surface film, the new cell shows a greater percentage of surface film formation than the cell cycled at 55 Hz, even though the latter had undergone testing for 6 months. Because the cell performance does not improve in the same period, its inclusion skews subsequent results. Therefore, the values recorded in Fig. 8 discount the Li-C peak as contributing to surface film even though it is not graphite active material.

Fig. 7 shows the formation of esters (O-C = O) and ethers (C-O). This is consistent with the chemical reduction of the electrolyte solvents at the surface of the negative electrode. An increase in the concentration of these compounds is consistent with surface film formation [18]. Fig. 8 shows that the concentration of surface film increases with the AC frequency used. However, the cell subject to 55 Hz has only 19% surface film compared to 35% at 10 Hz; due to lower concentrations of both O-C = O and C-O components (Fig. 7). The cell cycled at 14.8 kHz contains much higher concentrations of surface film, primarily due to increases in chemical components at binding energies consistent with an O-C = O chemical environment.

These results establish a dependency of passivating film growth on the frequency of an AC perturbation. Based on XPS analysis alone the worst cycling condition for cells is at high frequencies, reducing to have less impact at lower frequencies. However, there is a perceived anomaly at or around 55 Hz.

Thus far, electrochemical modelling results presented in Section 3, suggest that heat generation within the cell is related to the AC excitation frequency of a current load. Long term ageing test results for cells cycled under a number of AC and DC coupled waveforms show that capacity and power fade is progressively more pronounced for higher AC excitation frequencies. XPS results

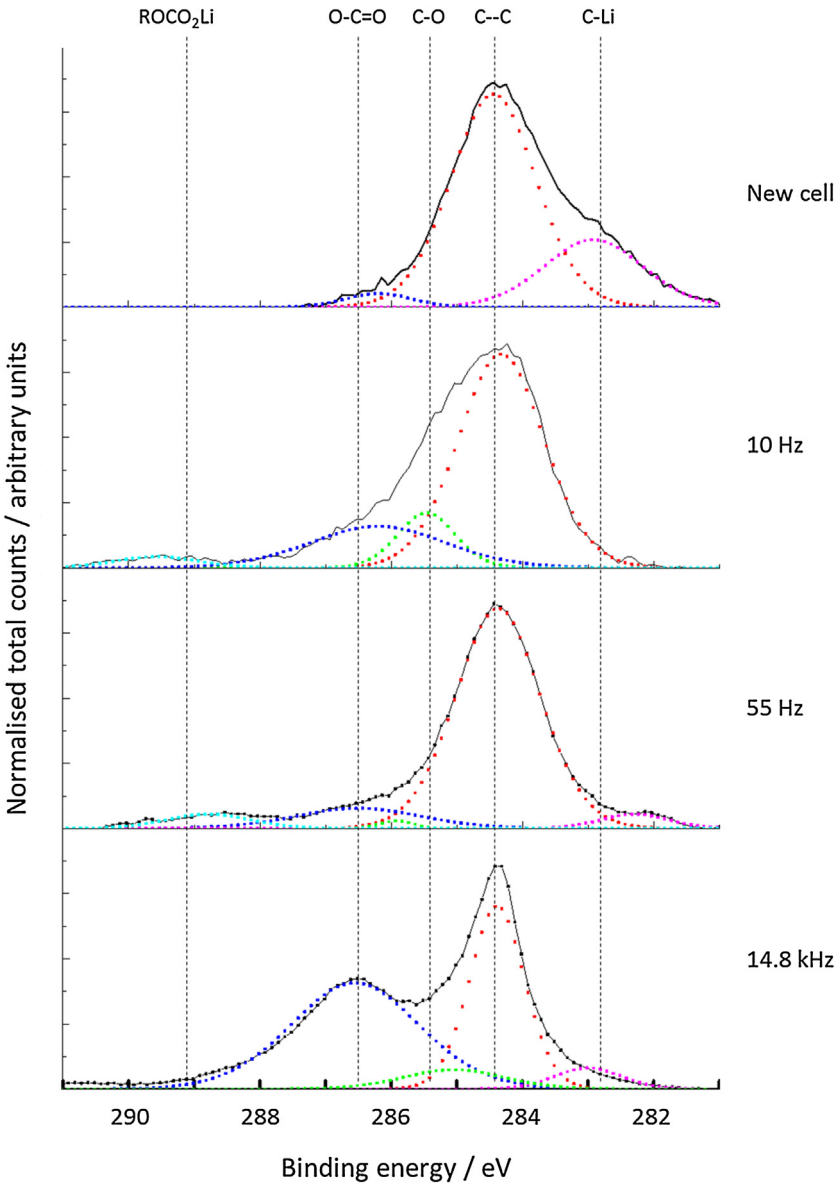

Fig. 7. XPS analysis results of the C 1s spectrum of a new cell and three cells subjected to 1200 DC cycles with different imposed AC frequencies (10 *Hz*, 55 *Hz* and 14.8 *kHz*) with the results of peak fitting showing possible chemical states (C-C, C-O. C-Li, O-C = O and $ROCO_2Li$).

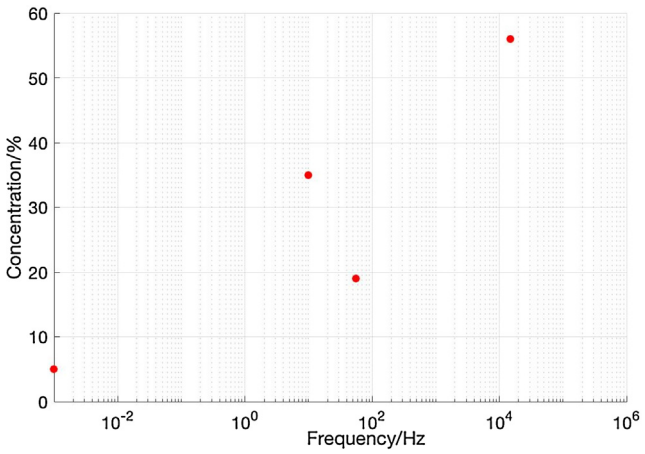

Fig. 8. Percentage concentration of the surface film (non C-C or C-Li peaks) from the data shown in Fig. 7. The data point at 0 Hz corresponds to a pristine cell.

corroborate this finding and further establishes that the pertinent mode of degradation is the growth of passivating films on the negative electrode. Thus, a causal link is proposed between frequency dependant heat generation and SEI film formation. In the following subsections therefore, results and discussion relating to heat generation within the lithium-ion cells is presented.

4.3. Cell Surface Temperature Measurements

It is well established that the growth of the SEI layer is strongly dependent on the temperature [8]. The difference in cell surface temperature resulting from the various current waveforms considered in this work is shown in Fig. 9. The differences in cell surface temperature resulting from superpositioning AC harmonics is qualitatively aligned with cell ageing results presented in Section 4.1 and with the growth of surface film measured from XPS results presented in Section 4.2. More specifically, a 55 Hz excitation exhibited the lowest cell

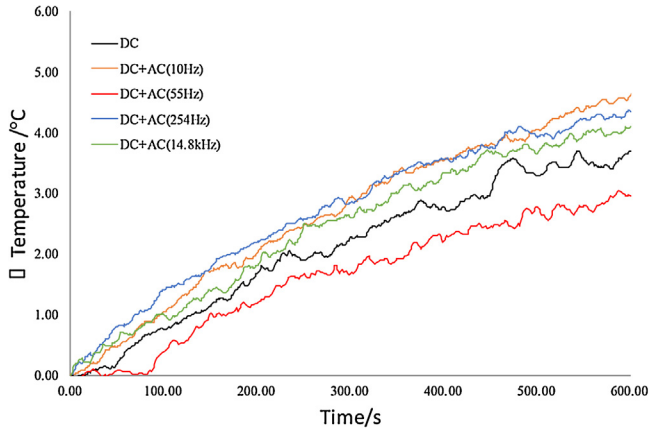

Fig. 9. Showing cell surface temperature rise under a 600 second discharge using the different current waveforms considered in this work.

temperature (see Fig. 9) in agreement with XPS results that showed least surface film growth at this excitation frequency (see Fig. 8).

4.4. Heat Generation Within Cells

There are four sources of heat generation in a lithium ion battery under operation, which include: heat generated from resistive dissipation, the entropy of the cell reaction, side reactions and the heat of mixing. The energy balance for the electrochemical system is expressed as [27]:

$$\dot{Q} = I(\phi_s - \phi_e - U) + IT\frac{\partial U}{\partial t} + \sum_i \Delta H_i^{avg} r_i + \int \sum_j \sum_k \left(\overline{H}_{jk} - \overline{H}_{jk}^{avg}\right)\frac{\partial c_{jk}}{\partial t} dv \quad (18)$$

The first term on the right-hand side of equation (18) $I(\phi_s - \phi_e - U)$ represents irreversible resistive dissipation caused by the deviation of the surface overpotential which is the difference between the solid phase potential (ϕ_s) and electrolyte phase potential (ϕ_e) from the volume averaged open circuit potential (OCP) due to a resistance of the passage of current (I). This term differs with that of Ref. [27] in that the heat generated by cell tabs are not considered. The second term is the reversible rate of heat generation due to electrochemical reactions, defined as $IT\frac{\partial U}{\partial t} = T\frac{\partial S}{\partial t}$ where S is the total entropy of the system and T is the bulk cell temperature. The third term is the heat arising from chemical side reactions where the enthalpy and rate of chemical reaction i is ΔH_i^{avg} and r_i respectively. The last term is the heat of mixing due to the formation and subsequent relaxation of concentration gradients, where c_{jk} is the concentration of species j in phase k, $\overline{H}_{jk}$ and $\overline{H}_{jk}^{avg}$ are the partial molar enthalpy and averaged partial molar enthalpy of species j in phase k respectively, and dv is the differential volume element.

The magnitude of heat generated by resistive dissipation and entropic reaction are comparable [27]. In Fig. 10 we present the impedance of the cell which quantifies resistive dissipation which, at a cell level, can be represented as $I^2 Z_{\text{cell}}$. The entropic contribution to heat generation is quantified through change in entropy $\frac{\Delta S}{nF} = \frac{\partial U}{\partial t}$ where n is the number of electrons involved in a half-cell reaction and F is the Faraday constant. Both of these terms are dependent on lithium concentration in the lattice, i.e., stoichiometry. Furthermore, while resistive dissipation is always exothermic, in principle entropic heat can be either exothermic or endothermic, depending on the entropy of the reaction and the direction of current and SoC.

The resistance (real part of the impedance) in Fig. 10 shows that battery impedance is frequency dependent and consequently heat generation within the battery will be a function of excitation frequency. In agreement with electrical results presented in Section 3, the 14.8 *kHz* excitation frequency is shown to have a higher resistance value than a current perturbation at 10 *Hz* which itself has a higher resistance than a 55 *Hz* AC waveform. This corroborates the cell surface temperature results presented in Fig. 9 and explains why 55 *Hz* resulted in less passivating film formation. In the Bode phase plot, the peak occurring close to 10^5 *Hz* corresponds to the surface film. SEI film growth occurs at both boundaries of the SEI [17,28], although the seperator side growth may be dominant. Under elevated temperatures the rate of SEI film growth at both boundaries is increased. For the inner SEI boundary, this occurs because the diffusivity (D) of ions is less hindered at elevated temperatures. This temperature dependency is described

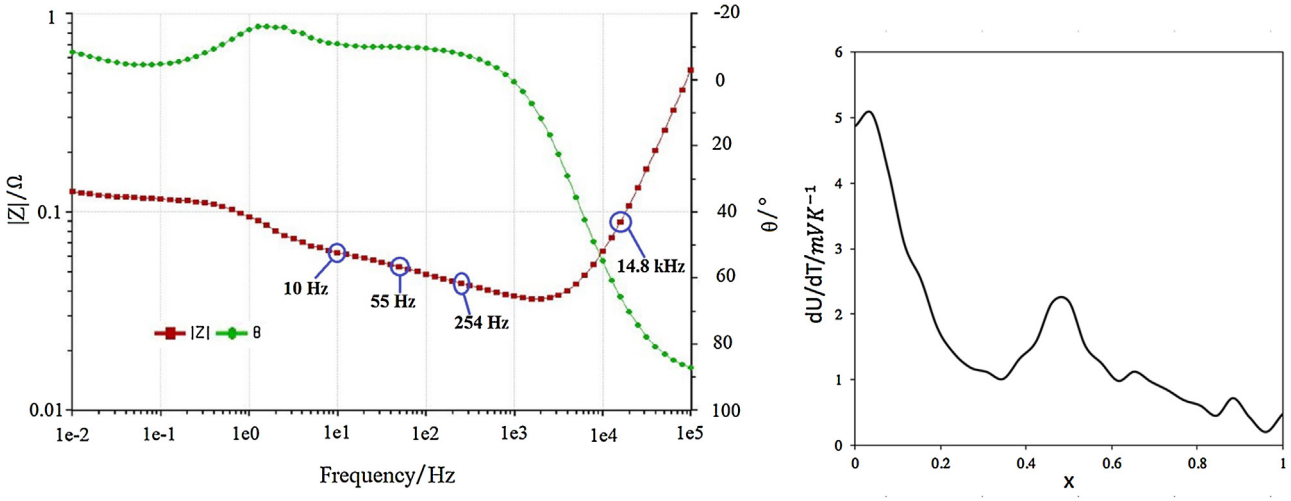

Fig. 10. The left hand panel shows a Bode phase plot illustrating cell resistance (|Z|) and phase (θ) as a function frequency for a pure AC waveform. The right hand panel shows the entropy as a function of stoichiometry.

by the Arrhenius correction,

$$D = D_{ref}\left[-\frac{E_{act}}{R}\left(\frac{1}{T_{ref}}-\frac{1}{T}\right)\right] \quad (19)$$

where E_{act} is the activation energy. The Bode phase plot also shows a short plateau region between the frequency limits 10^{-2} – 10^{-1} *Hz* corresponding to the semi-infinite diffusion region.

Cell surface temperature measurements presented in Fig. 9 suggest that heat generation within a cell is related to the AC excitation frequency. Equation (18) proposes four sources of heat generation, namely resistive dissipation, electrochemical reactions, chemical reactions and the heat of mixing. Impedance spectroscopy results presented in Fig. 10 show that resistive dissipation within the cell is frequency dependant. In the next subsection, a reference electrode cell potential relaxation experiment is employed to investigate the heat of mixing. Cell potential relaxation is indicative of ion concentration at the electrode-electrolyte boundary, such that a relatively longer relaxation time represents higher ion concentration. If there is a significant difference in ion concertation at the electrode-electrolyte boundary when different excitation frequencies are applied, this will reveal an underlying frequency dependence of the heat of mixing. Furthermore, assuming first-order solvent decomposition kinetics, a higher reactant concentration at the negative electrode boundary will, itself, facilitate an increased rate of SEI growth [29].

4.5. Cell Potential Relaxation Experiment Results

In an electrochemical system that is constantly perturbed, thermodynamic properties are determined by how the chemical distribution responds to changes. The rate of change of enthalpy (H) of the system is given by

$$\frac{dH}{dt} = \dot{Q} - IV. \quad (20)$$

In Fig. 11, the electrode potential after a 60 second DC step current of 0.1 mA/cm^2 superpositioned with an AC perturbation of frequencies 10 *Hz*, 55 *Hz*, 254 *Hz* and 14.8 *kHz* is shown. The correlation between the electrode potential and surface concentration is given by

$$\Delta\phi = (1-t_+)\frac{RT}{F}\ln\left(\frac{c_e|)_{x=L_-^e}}{c_s|)_{x=x'}}\right) \quad (21)$$

where $c_e|_{x=L_-^e}$ is the concentration of electrolyte at the surface of the negative electrode and $c_s|_{x=x}$ is the concentration of lithium at $x = x'$ in the negative electrode [30]. A slower cell potential relaxation therefore indicates a higher surface concentration and consequently a more pronounced growth rate of SEI through: 1) the heat of mixing, and 2) a larger ion concentration gradient.

The cell potential relaxation for a coupled DC and AC load with varying excitation frequencies, shown in Fig. 11, displays negligible differences between the waveforms. This suggests that the heat of mixing will not be a significant distinguishing factor. The cell potential relaxation result also suggests that the concentration of the reacting electrolyte species at the electrolyte-electrode interface is not the reason for intensified SEI formation at higher frequencies.

5. Conclusion

This paper has studied the causality of increased cell performance degradation due to superimposing current ripple on DC loads. In particular, the relationship between the frequency of an AC perturbation and the resulting battery degradation measured. Firstly, equation (16) established that for a current load of the form $I = I_{DC} + I_{AC}\sin(\omega t)$ the cell energy throughout is higher than when $I_{AC} = 0$ indicating that, just from an energy throughout perspective, superpositioning an AC perturbation will lead to increased degradation. Secondly, XPS results provide explicit evidence showing that the mechanism of degradation is the increased growth of surface film. In addition, XPS results highlight a dependency of surface film formation on the frequency of the coupled AC perturbation, corroborating the electrical ageing characterisation data. Using a heterogeneous electrochemical model, the frequency dependent formation of surface film was attributed to heat generation within the double layer, where ion dynamics is governed by the Poisson-Boltzmann equation. This causality of battery degradation, i.e., the prominence of resistive dissipation and its frequency dependence, was established by measuring cell surface temperature for different current waveforms (i.e., varying frequency ω). The results agreed with both electrical ageing characterisation and autopsy results. The processes that generate heat within the cell were also discussed. Resistive dissipation was explicitly shown to be frequency dependent and the distinguishing factor in heat generation under high frequency superpositioned AC loads. In conclusion, if an AC perturbation is coupled to a DC waveform, the rate of SEI growth is more pronounced. The increased SEI growth is related to increased resistive dissipation which is dependent on the frequency of the AC perturbation.

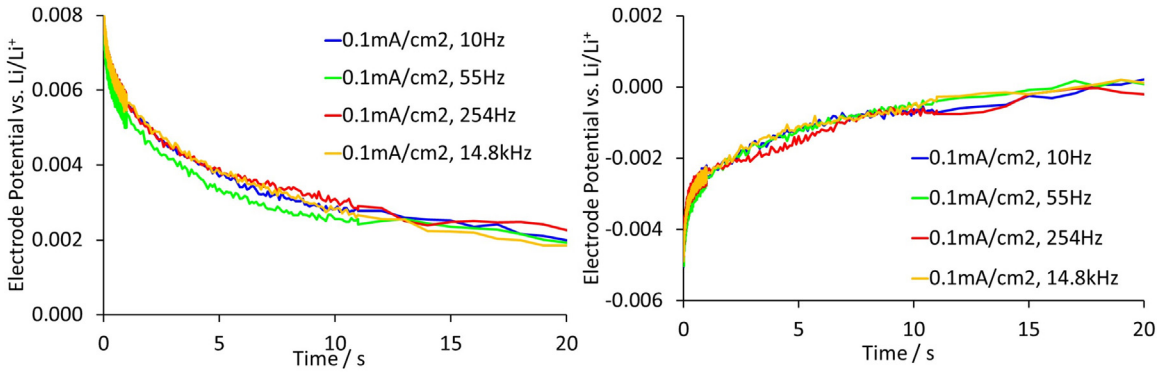

Fig. 11. Reference electrode tests on a lithium electrode showing cell potential relaxation during discharging (left hand panel) and charging (right hand panel) for various frequencies of AC perturbations.

5.1. Further Work

A number of opportunities exist where the research presented here may be further extended and refined. The results collected from both long term cycling experiments and autopsy studies suggest that degradation–for the cell specimen considered in this work–is lowest when an AC perturbation of 55 Hz, corresponding to the frequency exhibiting the lowest cell impedance in EIS results, is applied. More experimental and theoretical work is required to understand the precise nature of this effect and whether this finding can be extended to other battery technologies and cell types (i.e., other than NCA/C_6 and 18650-tyoe cells).

The second area of further work, is to reduce the potential impact of cell-to-cell variations (c.f., Fig. 5) by expanding the scope of the experimental study to encompass a greater number of cells of a given type. Expanding the experimental programme should also include using cells from a broader cross-section of manufacturers and chemistries. This will identify if the experimental results presented here and in Ref. [7] are transferable to other cell technologies.

In the work presented here (and in Ref. [7]), isolated AC perturbations are considered. In reality, as is shown in Fig. 1, there is a coupling of multiple AC perturbations. An experimental study on the impact of such complex couplings between DC and multiple frequency AC perturbations are required. Such an experimental study should also assess the relative degradation associated with varying the peak–peak amplitude of the AC current waveform in addition to the excitation frequency.

Finally, given that the aim of this study was to assess the causality and impact of varying frequency for AC current perturbations, further research should be undertaken to develop and validate prognostic ageing models which are able to quantify the gradation.

Acknowledgements

This research was supported by EPSRC grants (EP/M507143/1) and (EP/N001745/1) and the WMG Centre High Value Manufacturing Catapult (funded by Innovate UK) in partnership with Jaguar Land Rover (JLR).

Appendix A. Appendix

	Negative Electrode	Separator	Positive Electrode
Thickness δ (cm)	50×10^{-4}	25.4×10^{-4}	36.4×10^{-4}
Particle radius, Λ_s (cm)	1×10^{-4}		1×10^{-4}
Active material volume fraction	0.580		0.500
Electrolyte phase volume fraction ε_e	0.332	0.5	0.330
Maximum solid phase concentration $c_{s,max}$(mol cm^{-3})	16.1×10^{-3}		23.9×10^{-3}
Stoichiometry at 0% SOC	0.126		0.936
Stoichiometry at 100% SOC	0.676		0.442
Average electrolyte concentration c_e (mol cm^{-3})	1.2×10^{-3}	1.2×10^{-3}	1.2×10^{-3}
Exchange current density j_0 (A cm^{-3})	3.6×10^{-3}		2.6×10^{-3}
Charge-transfer coefficients α_a, α_c	0.5, 0.5		0.5, 0.5
SEI layer film resistance, Ω_{SEI} (Ω cm^2)	100		100
Solid phase Li diffusion coefficient, D_s (cm^2 s^{-1})	2×10^{-12}		3.7×10^{-12}
Solid phase conductivity, σ (S cm^{-1})	1.0		0.1
Electrolyte phase Li^+ diffusion coefficient, D_e (cm^{-2} s^{-1})	2.6×10^{-6}	2.6×10^{-6}	2.6×10^{-6}
Bruggeman porosity exponent, p	1.5	1.5	1.5
Electrolyte activity coefficient, $f^{\pm}$	1.0	1.0	1.0
Reference cell potential U_{ref} (V)	0		0
Molecular weight M_p (kg mol^{-1})	7.3×10^4		
Density of SEI Layer ρ_e (kg cm^{-3})	2.1×10^{-3}		
Side reaction exchange current density j_{0s} (A cm^{-3})	1.5×10^{-12}		
Conductivity of SEI Layer κ_p (S cm^{-1})	1×10^{-4}		
Density of electrolyte ρ_e (kg cm^{-3})	1123×10^6	1123×10^6	1123×10^6
Density of solid phase ρ_s (kg cm^{-3})	1343×10^6		2328.5×10^6
Electrolyte thermal Conductivity λ_e (W cm^{-1} K^{-1})	3.39×10^{-2}	3.39×10^{-2}	3.39×10^{-2}
Solid phase thermal conductivity λ_s (W cm^{-1} K^{-1})	3.39×10^{-2}		3.39×10^{-2}
Cation mobility β_+	3.24×10^{-10}	3.24×10^{-10}	3.24×10^{-10}
Anion mobility β_+	1.85×10^{-10}	1.85×10^{-10}	1.85×10^{-10}

References

[1] M. Armand, J.-M. Tarascon, Building better batteries, Nature 451 (7179) (2008 Feb) 652–657.
[2] B. Scrosati, et al., Lithium-ion batteries. A look into the future, Energy Environ. Sci. 4 (9) (2011) 3287.
[3] T. Hutchinson, S. Burgess, G. Herrmann, Current hybrid-electric powertrain architectures: Applying empirical design data to life cycle assessment and whole-life cost analysis, Appl. Energy 119 (2014) 314–329.
[4] D.M. Erickson, W. Robert, Fundamentals of power electronics, Springer Science & Business Media, 2007.
[5] M. Yilmaz, P.T. Krein, Review of Battery Charger Topologies, Charging Power Levels, and Infrastructure for Plug-In Electric and Hybrid Vehicles, IEEE Trans. Power Electron. 28 (5) (2013 May) 2151–2169.
[6] C. Mi, F.Z. Peng, K.J. Kelly, and V. Hassani, "Topology, design, analysis and thermal management of power electronics for hybrid electric vehicle applications," *J. Electr. Hybrid Veh.*, 1(3), pp. 276-294.
[7] K. Uddin, A.D. Moore, A. Barai, J. Marco, The effects of high frequency current ripple on electric vehicle battery performance, Appl. Energy 178 (2016) 142–154.
[8] J. Vetter, P. Novák, M.R. Wagner, C. Veit, K.-C. Möller, J.O. Besenhard, M. Winter, M. Wohlfahrt-Mehrens, C. Vogler, A. Hammouche, Ageing mechanisms in lithium-ion batteries, J. Power Sources 147 (1) (2005) 269–281.
[9] L. Somerville, J. Bare, S. Trask, P. Jennings, A. McGordon, C. Lyness, I. Bloom, The effect of charging rate on the graphite electrode of commercial lithium-ion cells: A post-mortem study, J. Power Sources 335 (2016) 189–196.
[10] D. Andre, C. Appel, T. Soczka-Guth, D.U. Sauer, Advanced mathematical methods of SOC and SOH estimation for lithium-ion batteries, J. Power Sources 224 (2013) 20–27.
[11] M. Ecker, N. Nieto, S. Käbitz, J. Schmalstieg, H. Blanke, A. Warnecke, D.U. Sauer, Calendar and cycle life study of Li(NiMnCo)O2-based 18650 lithium-ion batteries, J. Power Sources 248 (2014) 839–851.
[12] A. Farmann, W. Waag, A. Marongiu, D.U. Sauer, Critical review of on-board capacity estimation techniques for lithium-ion batteries in electric and hybrid electric vehicles, J. Power Sources 281 (2015) 114–130.
[13] R. Spotnitz, Simulation of capacity fade in lithium-ion batteries, J. Power Sources 113 (1) (2003) 72–80.
[14] S. Bourlot, P. Blanchard, S. Robert, Investigation of aging mechanisms of high power Li-ion cells used for hybrid electric vehicles, J. Power Sources 196 (16) (2011) 6841–6846.
[15] R. Dedryvère, S. Laruelle, S. Grugeon, L. Gireaud, J.-M. Tarascon, D. Gonbeau, XPS Identification of the Organic and Inorganic Components of the Electrode/Electrolyte Interface Formed on a Metallic Cathode, J. Electrochem. Soc. 152 (4) (2005) A689.
[16] S. Leroy, F. Blanchard, R. Dedryvère, H. Martinez, B. Carré, D. Lemordant, D. Gonbeau, Surface film formation on a graphite electrode in Li-ion batteries: AFM and XPS study, Surf. Interface Anal. 37 (10) (2005 Oct) 773–781.
[17] D. Aurbach, Review of selected electrode–solution interactions which determine the performance of Li and Li ion batteries, J. Power Sources 89 (2) (2000) 206–218.
[18] D. Aurbach, Y. Talyosef, B. Markovsky, E. Markevich, E. Zinigrad, L. Asraf, J.S. Gnanaraj, H.-J. Kim, Design of electrolyte solutions for Li and Li-ion batteries: a review, Electrochim. Acta 50 (2) (2004) 247–254.
[19] M. Doyle, J. Newman, The use of mathematical modeling in the design of lithium/polymer battery systems, Electrochim. Acta 40 (13–14) (1995 Oct) 2191–2196.
[20] J.S. Newman, K.E. Thomas-Alyea, Electrochemical systems, J. Wiley, 2004.
[21] K. Smith, C.-Y. Wang, Solid-state diffusion limitations on pulse operation of a lithium ion cell for hybrid electric vehicles, J. Power Sources 161 (1) (2006 Oct) 628–639.
[22] K. Uddin, S. Perera, W. Widanage, L. Somerville, J. Marco, Characterising Lithium-Ion Battery Degradation through the Identification and Tracking of

Electrochemical Battery Model Parameters, Batteries 2 (2) (2016 26-Apr) 13 Multidisciplinary Digital Publishing Institute,.
[23] P. Ramadass, B. Haran, P.M. Gomadam, R. White, B.N. Popov, Development of First Principles Capacity Fade Model for Li-Ion Cells, J. Electrochem. Soc. 151 (2) (2004) A196.
[24] M. Xiao, S.-Y. Choe, Impedance model of lithium ion polymer battery considering temperature effects based on electrochemical principle: Part I for high frequency, J. Power Sources 277 (2015 Mar) 403–415.
[25] D.C. Grahame, The Electrical Double Layer and the Theory of Electrocapillarity, Chem. Rev. 41 (3) (1947 Dec) 441–501.
[26] M. Lu, H. Cheng, Y. Yang, A comparison of solid electrolyte interphase (SEI) on the artificial graphite anode of the aged and cycled commercial lithium ion cells, Electrochim. Acta 53 (9) (2008) 3539–3546.
[27] K.E. Thomas, J. Newman, Thermal Modeling of Porous Insertion Electrodes, J. Electrochem. Soc. 150 (2) (2003) A176.
[28] Y. Choquette, G. Brisard, M. Parent, D. Brouillette, G. Perron, J.E. Desnoyers, M. Armand, D. Gravel, N. Slougui, Sulfamides and Glymes as Aprotic Solvents for Lithium Batteries, J. Electrochem. Soc. 145 (10) (1998) 3500.
[29] M.B. Pinson, M.Z. Bazant, Theory of SEI Formation in Rechargeable Batteries: Capacity Fade, Accelerated Aging and Lifetime Prediction, J. Electrochem. Soc. 160 (2) (2012 Dec) A243–A250.
[30] Q. Wang, H. Li, X. Huang, L. Chen, Determination of Chemical Diffusion Coefficient of Lithium Ion in Graphitized Mesocarbon Microbeads with Potential Relaxation Technique, J. Electrochem. Soc. 148 (7) (2001) A737.